Available online at www.sciencedirect.com

SciVerse ScienceDirect

Ceramics International 39 (2013) 4861–4875

CERAMICS INTERNATIONAL

www.elsevier.com/locate/ceramint

Microstructure of seal formed between a Nb wire and an Al_2O_3 capillary melted by YAG laser radiation

Takuya Honma[a,*], Hiroshi Kamata[a], Junichi Tatami[b]

[a]*Research & Development Center, Toshiba Lighting & Technology Corporation, 1-201-1 Funakoshi, Yokosuka, Kanagawa 237-8510, Japan*
[b]*Graduate School of Environment and Information Sciences, Yokohama National University, 79-7 Hodogayaku, Yokohama, Kanagawa 240-8501, Japan*

Received 22 August 2012; received in revised form 23 November 2012; accepted 23 November 2012
Available online 1 December 2012

Abstract

Cracks occasionally develop inside the glass frit, the sealing material used in ceramic metal-halide lamps that employ polycrystalline alumina as the arc-tube material, although the rate at which these cracks develop is low. Therefore, we proposed a new method to stop their development. Our method did not make use of a glass frit and involved the formation of a seal between the Nb wire and the Al_2O_3 capillary melted by the radiant energy from a YAG laser. However, cracks or voids developed inside the melted Al_2O_3 capillary. Therefore, in order to control the Al_2O_3 microstructure inside the melted Al_2O_3 capillary and thus to obtain a better seal, grain growth was suppressed by combining the processes of annealing after melting and grain-boundary deposition of Ta. The Al_2O_3 microstructure could be controlled by these factors. Thus, optimized conditions for forming the seal were achieved.

Keywords: B. Grain size; B. Microstructure; C. Thermal conductivity; D. Al_2O_3

1. Introduction

In recent years, high-intensity discharge lamps have achieved higher luminance levels. Because of this trend, the operating temperatures of the lamp arc tubes have also increased. Conventionally, silica glass has been used as an arc-tube material. However, because of its glass-transition point of 1150 °C, the operating temperatures of these lamps were limited. For this reason, since the early 1980s, polycrystalline alumina (PCA) has been used as an alternative arc-tube material in metal-halide lamps, which employ metal halides for luminosity [1,2]. The use of PCA made it possible to achieve operating temperatures above 1150 °C, thus resulting in higher luminance levels. However, in the seals of such lamps, cracks develop inside the glass frit, which is the sealing material, although the rate of their development is low. The seal is composed of a glass frit (Al_2O_3–Dy_2O_3–SiO_2), an electrode system (W electrode–Mo wire–Nb wire), and an Al_2O_3 capillary, as shown in Fig. 1. An Al_2O_3 capillary exists at either ends of the arc tube and is made of polycrystalline alumina. The principal reason for using the Nb wire is that its coefficient of thermal expansion (CTE) is closer than that of other metals to the CTE of the Al_2O_3 capillary. Therefore, the Nb wire is used in the electrode system to keep the arc tube airtight. Nevertheless, cracks occasionally develop inside the glass frit. The development of these cracks is influenced by the seal stress, which is affected by the difference in the CTE of the parts that compose the seal. The CTE of the glass frit is different from those of the Al_2O_3 capillary and the Nb wire. Consequently, seal stress is generated, and the possibility of a crack developing inside the glass frit increases further. As a measure against this, cermet, a conductive material that is a composite of Mo and $A1_2O_3$, has been used in place of the Nb wire [1,3]. However, the inhibitory effect of using cermet is not sufficient to stop the development of the cracks.

Earlier studies investigating the seals of ceramic metal-halide lamps have mainly considered the CTE of the glass frit, along with its crystal structure and its strength [4–11].

Abbreviations: BSE, back-scattered electron; CTE, coefficient of thermal expansion; EPMA, electron probe microanalyzer; PCA, polycrystalline alumina.

*Corresponding author. Tel.: +81 46 862 2154; fax: +81 46 860 1203.
E-mail address: takuya.honma@tlt.co.jp (T. Honma).

0272-8842/$ - see front matter © 2012 Elsevier Ltd and Techna Group S.r.l. All rights reserved.
http://dx.doi.org/10.1016/j.ceramint.2012.11.079

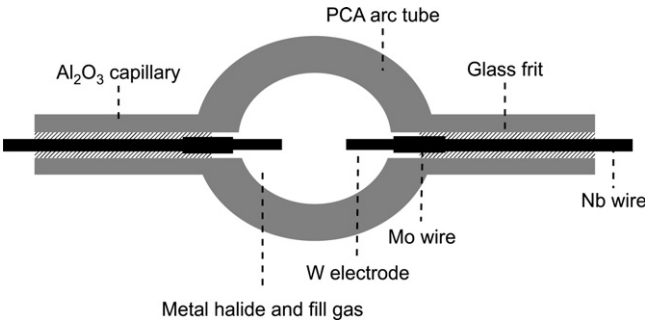

Fig. 1. Ceramic metal-halide lamp.

However, these studies have not led to the development of solutions to prevent cracks. In addition, as the glass transition point of the glass frit is around 870 °C, it is necessary to keep the distance between the tip of the electrode, where the temperature is the highest in the lamp, and the seal constant when the lamps are being designed. Therefore, eliminating the use of glass frits would also do away with this restriction. The elimination would also help with the miniaturization of lamps and allow for an increase in the operating temperatures of the lamps, leading to higher luminance levels. Until now, solid-phase bonding has been studied with respect to bonds between ceramics and metals such as Al_2O_3 and Nb [12], but bonding by melting has not yet been investigated.

In this study, we proposed a new method of directly sealing a Nb wire with an Al_2O_3 capillary melted using radiant energy from a YAG laser, without making use of a glass frit. However, cracks and voids developed inside the Al_2O_3 melted capillary. Therefore, in order to obtain a better seal, grain growth was suppressed by a combination of annealing after melting and grain boundary deposition using Ta, which is a metal with a high melting point.

2. Experimental procedure

An electrode system was inserted into the Al_2O_3 capillary, which was melted by the YAG laser radiation to form the seal. The seal was achieved using a Nb wire as there was a small difference in the CTEs of the glass frit and the Al_2O_3 capillary.

The Al_2O_3 capillary used in this study was made of polycrystalline alumina (G-40, NGK Insulators, Ltd.), and its grains, shown in Fig. 2, were isotropic with an average grain size of 35 μm. The Al_2O_3 capillary had an outer diameter of 1.80 mm, thickness of 0.50 mm, and length of 8.00 mm. As for the Nb wire (NbZr (1%), W.C. Heraeus GmbH), 1 wt% of ZrO_2 had been added to Nb, and it was 10.00 mm in length and 0.69 mm in diameter. In addition, in order to eliminate the effects of the occluded gas that is discharged during heating by the laser, a vacuum heat treatment (1.33×10^{-4} Pa; 1500 °C; 1 h) was performed on the arc tube and electrode system.

For the melting of the Al_2O_3 capillary to form the seal, radiant energy from a YAG laser (ML-2550A, Miyachi

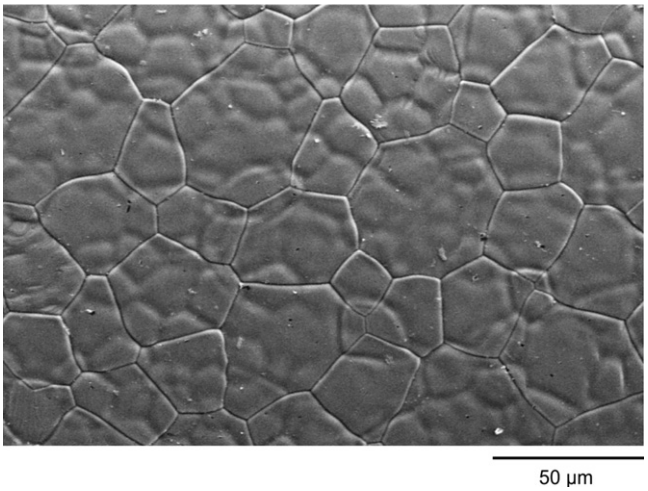

Fig. 2. SEM image of the grains in an Al_2O_3 capillary made of PCA.

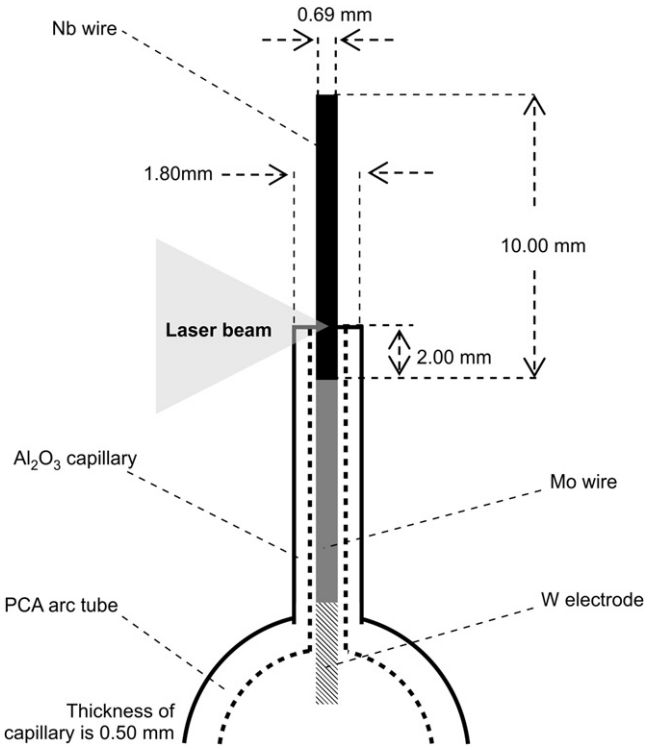

Fig. 3. Sample installation at the time of irradiation by a YAG laser.

Corp.) (output: 400 W; emission wavelength: 1.064 μm) was used. The sealing procedure was performed in a chamber filled with N_2 at a pressure of 0.27 MPa, as shown in Fig. 3, with the arc tube kept in an upright position and the electrode system inserted in the Al_2O_3 capillary. At that time, the inner surface of the Al_2O_3 capillary and the Nb wire were partly in contact with each other. The laser radiation was focused on the Nb wire protruding from the end of the Al_2O_3 capillary. The irradiated area had a diameter of 0.4 mm.

The sealing process consisted of two steps: the melting step and the cooling step. A rapidly-cooled sample

(Sample RC) was prepared without the additional cooling step, i.e., irradiation by the laser was halted after the melting step during the sealing process. The sample that underwent annealing (Sample AN) was prepared with annealing as an additional cooling step after the melting step during the sealing process. As for the sample with a Ta mesh foil wrapped around it (Sample TM), shown in Fig. 4, the foil was wrapped around the outer surface of the 2.00 mm end of the Al_2O_3 capillary and was heated by laser radiation. The thickness of the Ta mesh foil was 0.05 mm, the diameter of the holes was 0.50 mm, and the space between the holes was 0.20 mm. This sample was also prepared with an annealing step after the melting step during the sealing process, similarly to Sample AN. The structures of various samples that underwent the sealing process are detailed in Table 1, and the temperature profile used for the sealing process is shown in Table 2.

To investigate the internal microstructure of Al_2O_3 in the melted Al_2O_3 capillaries, the cross-section of each sample was observed. During manufacturing, the cross-sections were polished using Ar ion beam (SM-09010, JEOL Ltd.) along the axial direction. The samples were analyzed using an electron probe microanalyzer (EPMA) (JXA-8900, JEOL Ltd.) that had a back-scattered electron (BSE) detector and a system for mapping analysis attached. In addition to the existence of cracks and voids, the average grain size, the rate of random variations in grain size, and the aspect ratio and orientation of the grains of A_2O_3 in the melted Al_2O_3 capillary were also investigated. These results were quantified for numerical analysis using the recorded BSE images and an image analysis software (PopImaging, Version 4.00, Digital Being Kids Limited Company).

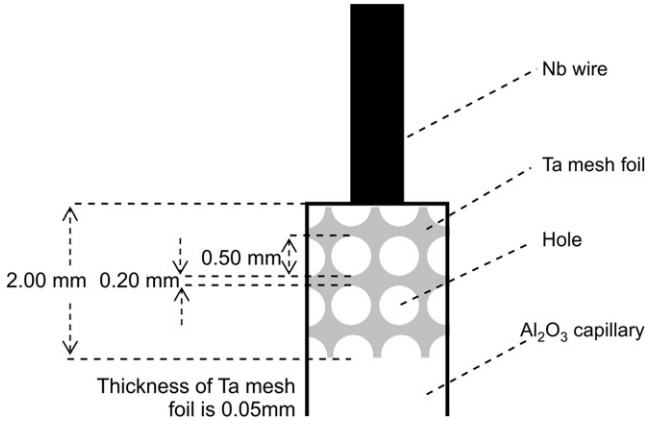

Fig. 4. Sample TM with the Ta mesh foil wrapped around it.

3. Results and discussion

3.1. Effects of rapid cooling on the crystal structure of Al_2O_3

The BSE images of the cross-section of Sample RC are shown in Fig. 5. There was a large void in the melted area. There were differences in the microstructures of the different zones, and these zones were classified into five categories labeled (A)–(E). The zones were defined as follows: (A) was the zone near the Nb wire; B was the zone between the Nb wire and the void; (C) was the zone near the void; (D) was the outer surface; and (E) was the zone near the unmelted area. The average grain size, grain size distribution, aspect ratio, and orientation of the grains of Al_2O_3 in the melted Al_2O_3 capillary were also quantified. As for the average grain size, the median grain diameter (D_{50}), located at the midpoint of the cumulative distribution of the diameter values calculated using the equivalent circle diameter values, was used. The rate of random variations in the grain size was calculated using the following formula.

$$\text{Rate of random variations in grain size} = (D_{90}\text{-}D_{10})/D_{50} \quad (1)$$

D_{90} represents the grain diameter located at 90% in the cumulative distribution, and D_{10} is the grain diameter

Table 2
Temperature profiles for the sealing processes performed on the various samples.

Sample	Melting process[a] Radiant energy ($W\,m^{-2}$)	Cooling process Cooling rate ($(W\,m^{-2})\,s^{-1}$)[b]
Sample RC	432	—[c]
Sample AN	432	6.5
Sample TM	396	5.9

[a]Samples are rapidly heated with a YAG laser.
[b]Data correspond to a change from the maximum value of radiant energies consumed (100%) during the melting process to 30% of that value.
[c]Sample is not annealed.

Table 1
Structure of the samples that underwent the sealing process.

Sample	Structure
Sample RC Sample AN	An electrode system is inserted into an Al_2O_3 capillary
Sample TM	A Ta mesh foil is wrapped around the outer surface of an Al_2O_3 capillary, and an electrode system is inserted into an Al_2O_3 capillary

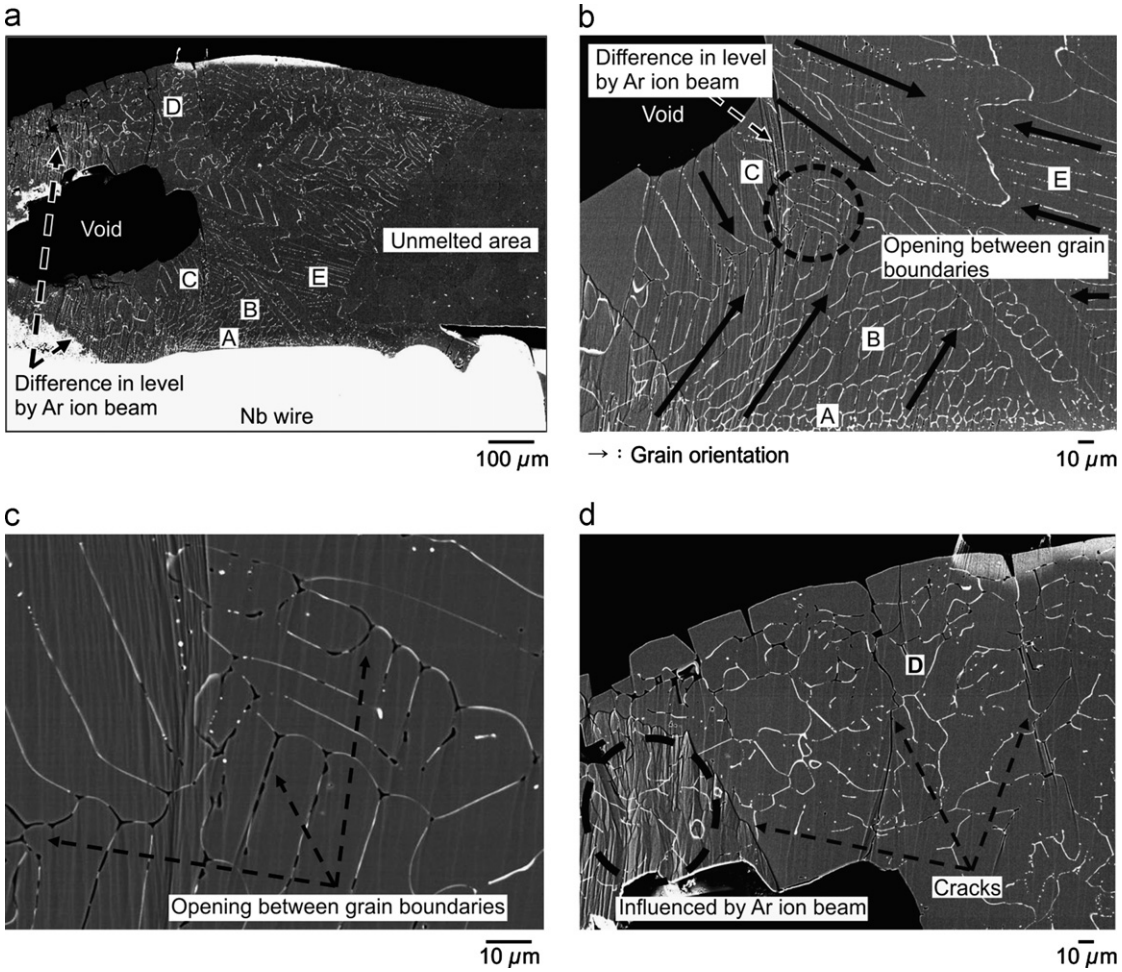

Fig. 5. BSE images of a cross-section of Sample RC. (a) Whole image, (b) circumference of void, (c) opening between grain boundaries and (d) outer surface.

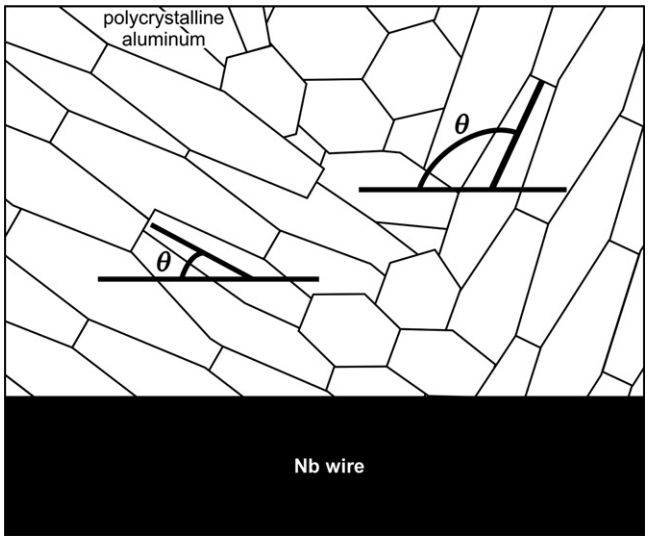

Fig. 6. Definition of grain orientation angle for grains of polycrystalline aluminum oxide.

located at 10%. This equation indicates that the smaller the calculated value is, the smaller the rate of random variations in the grain size would be. To investigate the aspect ratio, the ratio of the long axis of each grain and the short axis, which runs across the perpendicular as if it cuts the long axis in half, was calculated. Then, using this ratio, a 90% aspect ratio (α_{90}) was obtained. The ratio, α_{90}, can be described as follows: when the values of the ratio of the long and short axes are arranged in ascending order, α_{90} is the average of the values that at 90% or greater in the cumulative frequency distribution. Moreover,. Khangar et al. report that grains of Al_2O_3 grow along *C*-axis after laser irradiation [13]. Therefore, the orientation angle, shown in Fig. 6 and defined as the angle between the long axis (i.e, the *C*-axis) of each grain and the direction of the axis of the Nb wire, and its distribution is shown in Fig. 7. The values of the average grain size, rate of random variations in the grain size, and aspect ratios are given in Table 3.

Zone (A) exhibited small values for the average grain size, the rate of random variations in the grain size, and the aspect ratio of the investigated areas. The distribution of the orientation angles was wide. Zone (B) showed values for the average particle size that were larger than those for zone (A); however, the values of their rates of random variations in the grain size and aspect ratios were similar.

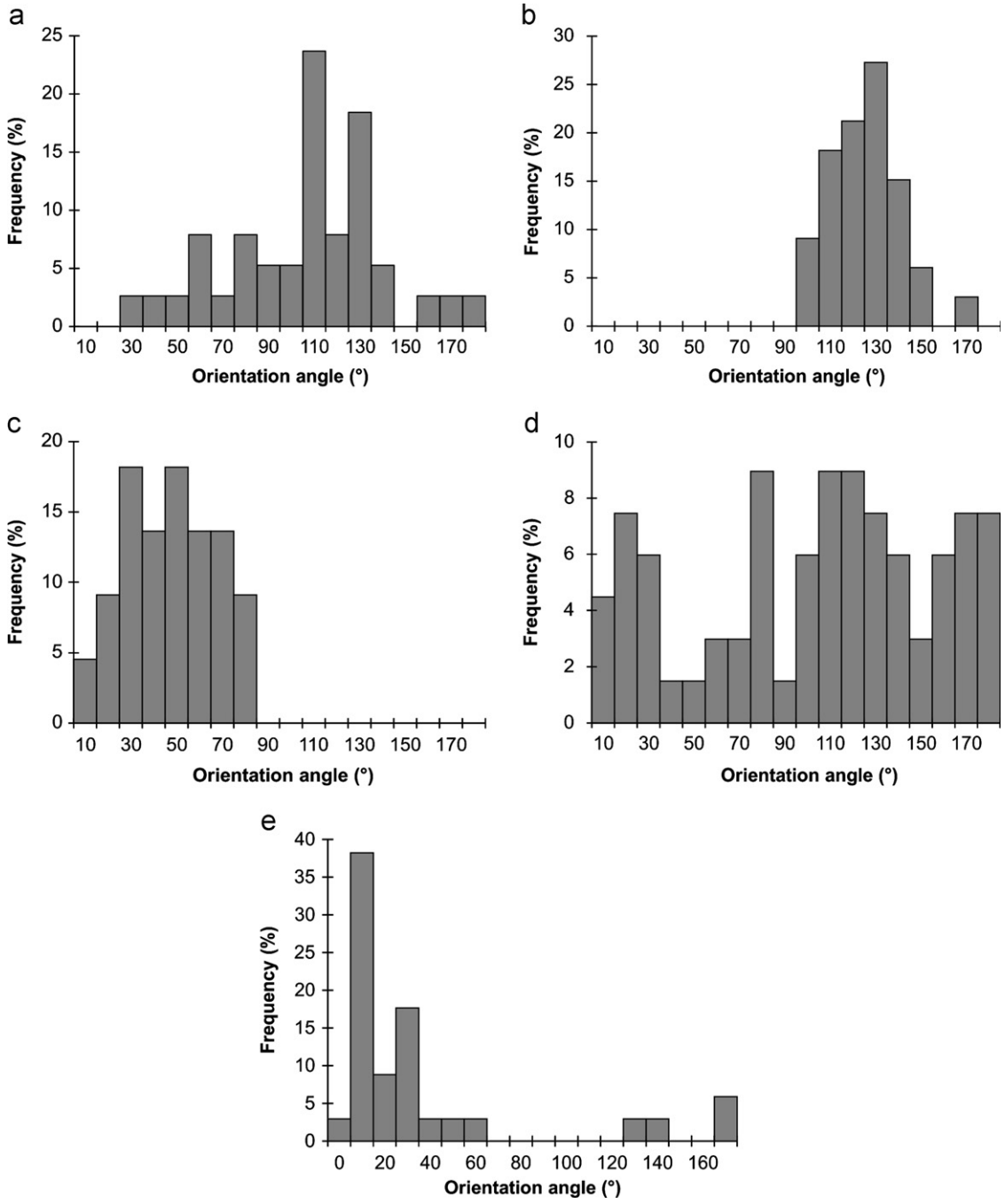

Fig. 7. Distribution of grain orientations in Sample RC. (A) Near the Nb wire, (b) Between the Nb wire and the void, (c) Near the void, (d) Outer surface, and (e) Near the unmelted area.

Table 3
Crystal structure of Sample RC.

Zone	Investigated area	Average grain size (μm)	Rate of random variations in the grain size	Aspect ratio
A	Nb wire circumference	6.6	1.0	2.5
B	Between Nb wire circumference and void circumference	15.2	0.7	3.2
C	Void circumference	268.1	1.5	6.5
D	Outer surface	18.3	2.0	3.3
E	Unmelted area	29.1	1.5	18.3

The distribution of the orientation angles was narrow, but it showed kurtosis around 130°, and its distribution was similar to that of zone (A), which showed kurtosis around 110°. For zone (C), the average grain size, the rate of random variations in the grain size, and the aspect ratio were large. In particular, the average particle size was much larger than those of the other zones. In addition, the distribution of the orientation angles was narrow. Zone (D) did not exhibit any irregular trend in average grain size and aspect ratio when compared to the other investigated zones. However, of all the zones investigated, the rate of random variations in the grain size was the largest for zone (D). In addition, the distribution for the orientation angles was wide. Zone (E) exhibited values for the average grain size, rate of random variations in the grain size, and aspect ratio that were relatively large compared to those of the other investigated zones. In particular, the aspect ratio was markedly larger. The distribution of the orientation angles was narrow. Furthermore, a white substance was seen to exist between the grain boundaries in the entire area that underwent melting. In particular, this substance existed in greater quantities near the Nb wire. The substance was investigated by a mapping analysis performed using an EPMA. The results, displayed in Fig. 8, showed that this white substance was Nb.

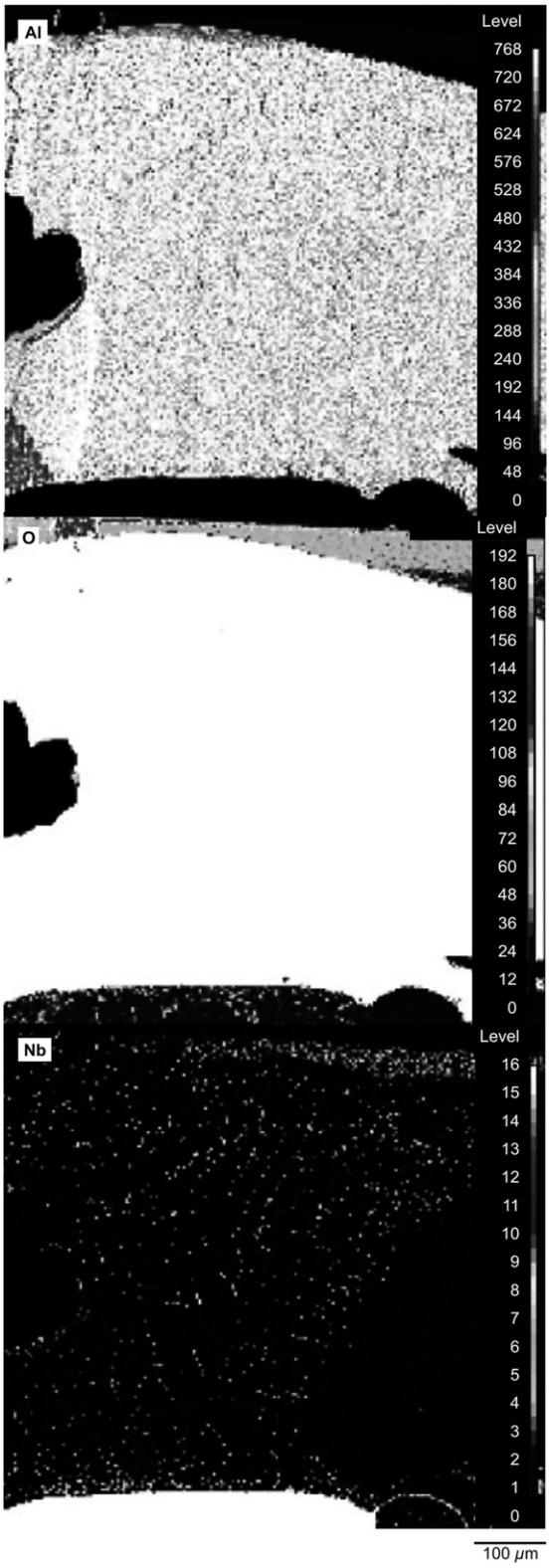

Fig. 8. Result of the EPMA-based analysis of the white substance found between the grain boundaries in Sample RC.

The reasons for the differences in the microstructures, as seen in Fig. 5, include the effects of the thermal conduction process during the sealing process by the radiant energy of the YAG laser, the existence of Nb at the grain boundaries, and the existence of voids in the inner portion of the melted Al_2O_3 capillary. The thermal conduction during the sealing process is explained below. The emission wavelength of the YAG laser is 1.064 μm, and the transmittance ratio of Al_2O_3 at this wavelength is 80% or greater [14]. For this reason, 80% or more of the radiant energy from the laser is transmitted and reaches the Nb wire without being absorbed into the Al_2O_3 capillary. During this process, a small fraction of the radiant energy that reaches the Nb wire is not absorbed by the Nb wire, but is reflected by it. The temperature of the Nb wire increases as a result of the energy absorbed, and heat is likely to be transmitted to the inner surface of the Al_2O_3 capillary by thermal conduction or radiation. To investigate whether heat is transmitted via conduction or radiation, the influence of the difference in the contact state between the Al_2O_3 capillary and the Nb wire, i.e., the influence of the contact state on the melting state of the Al_2O_3 capillary was investigated. The result showed that the melting state varied with the contact state. On the basis of this result, it is considered that melting of the Al_2O_3 capillary is more due to thermal conduction than radiation. Therefore, if thermal conduction contributes more to this temperature rise than radiation, heat will be transmitted from the Nb

Table 4
Properties of materials (at 300 K) [15–18].

Material	Melting point (°C)	Thermal conductivity (W/(m K))
Al_2O_3	2044	36.0
Nb	2468	53.7
Ta	2996	57.5

wire to the Al_2O_3 capillary relatively slowly, because the thermal conductivity of Al_2O_3 is lesser than that of Nb, as shown in Table 4 [15–18]. At the same time, when the radiant energy from the laser reaches the Nb wire and subsequently raises the temperature, Nb from the surface of the Nb wire evaporates and is deposited on the inner surface of the Al_2O_3 capillary. This allows the radiant energy from the laser to be absorbed and the temperature of the inner surface of the Al_2O_3 capillary to rise. Thermal conduction of heat from the inner to the outer surface of the Al_2O_3 capillary occurs mainly by these two processes, and the Al_2O_3 capillary melts. Then, after irradiation by the laser stops, cooling commences, and the outer surface of the melted area is cooled initially, followed by the Nb wire. In this case, as described above, the thermal conductivity of Nb is greater than that of Al_2O_3. However, the heat capacity of Al_2O_3 is greater because the weight of Al_2O_3 in the melted area is more. Therefore, cooling does not progress easily. The temperature of the Nb wire is also higher at the start of the cooling step because the Nb wire is the heat source. For this reason, it takes the Nb wire longer to cool.

The process of formation of the Al_2O_3 microstructure was determined, while considering the thermal conduction process described above. Zone (A) is the most distant from the outer surface of the melting area, and is located near the Nb wire, which is the heat source. Thus, of all the melted zones, cooling for zone (A) is the slowest. Because of this reason, an annealing effect took place during the cooling step, whereby the rate of random variations in the grain size was small, and the orientation angles tended toward a particular value. However, despite the annealing effect, the average particle size was smaller than those for the other zones in the melted area. This is chiefly due to the effect of Nb being present in the grain boundaries. This Nb has evaporated from the surface of the Nb wires because of the radiant energy from the laser and been deposited on the inner surface of the Al_2O_3 capillary. As the temperature of the Nb wire during evaporation is unknown, taking into consideration the melting points of $A1_2O_3$ and Nb, shown in Table 4, as well as the fact that the Al_2O_3 melted but the Nb wire did not, it is highly likely that the temperature of the Nb wire during evaporation may have reached a value in the range of 2044–2468 °C. In addition, the Nb deposited on the inner surface of the Al_2O_3 capillary was convected and diffused into the liquid-phase state of $A1_2O_3$ when the Al_2O_3 capillary melted and was deposited on the grain boundaries as the crystallization of Al_2O_3 progressed during the cooling step. At this stage, the deposited Nb acted as a grain growth retardant. In particular, as the amount of Nb deposition increased, the grain growth was inhibited more than in any other zones in the melted area, as shown in Fig. 8, because zone (A) is closest to the Nb wire. Moreover, it has been reported that Al_2O_3–Mo-based composite materials can take a columnar form because of the influence of Mo [19]. This is similar to the crystalline form observed not only at zone (A) but also at all the other zones in the melted area other than zone (D). Furthermore, it has also been reported that, upon melting of sintered Al_2O_3 by the radiant energy from a CO_2 laser, Al_2O_3 grains with a columnar form align in the direction of the thermal distribution, i.e., in the direction of the flow of heat energy around the irradiated area [20]. On the basis of these results, and given that the orientation of zone (A) from the Nb wire, the heat source, was toward the center of the melted area, we can assume that thermal distribution during the sealing process was aligned in this direction. This was identical to the direction of the thermal distribution predicted above. In addition, there is a high possibility that heterogeneous nucleation of Al_2O_3 occurred at the surface of the Nb wire in zone (A). It is considered that the heterogeneous nucleation occurs in the zones where the surface energy or interfacial energy is high. In Sample RC, in addition to the surface of the Nb wire in zone (A), nucleation also occurred at the inner surface of a void in zone (C) and the outer surface of the melted area in zone (D). Therefore, there is a possibility that, apart from being affected by the thermal distribution, the orientation of zone (A) was also influenced by the angle of the crystal plane of the grain nuclei generated by the heterogeneous nucleation.

Although the average grain size of zone (B) was larger than that of zone (A), it was smaller than that of the other zones in the melted area. The reason is that zone (B) was not located near the Nb wire as was the case for zone (A), even though zone (B) is closer to the Nb wire than the other zones in the melted area. Thus, the average grain size in zone (B) was influenced by the amount of Nb deposited, although it was not as high as that in the case of zone (A). In addition, zones (A) and (B) showed similar trends for all parameters other than the average grain size. The reason for this is that zones (A) and (B) differed only in the amount of Nb deposited, and the thermal conduction was similar for both.

Zone (C) exhibited an average grain size that was significantly larger than those for the other zones in the melted area. Moreover, the aspect ratio was also larger than those of the other zones. It is very likely that this was due to the presence of voids. Voids are formed by the gas generated during the melting step, including the occluded and melting gases emitted from $A1_2O_3$ and the occluded gases emitted from the Nb wire. The grain growth progressed because annealing took place in the periphery of zone (C) as these gases created an insulation effect during the cooling step. In addition, the amount of Nb deposited in zone (C), which acts as a grain growth inhibitor, was lower than in the case of zones (A) and (B), and this also lead to larger grain growth. With respect to the variations in the orientation of the grains, heterogeneous nucleation occurred on the inner surface of the void, and, grains grew on the basis of the angles of the crystal planes of these grain nuclei. As for the reason why this void remained behind, it is likely that the void was

unable to diffuse outside because the cooling rate of zone (D), located on the outer surface, is high, and solidification occurs quickly. Pores were observed at the triple points inside the grains in some parts of the melted area. The pores were attributable to the gases, i.e., the occluded and melting gases from $A1_2O_3$ and the occluded gases from the Nb wire emitted during the melting process, which were caused by gases that remained half-way through the grain-boundary diffusion process.

Meanwhile, cracks existed in zone (D). Its rate of random variations in the grain size was the largest among all the zones in the melted area, and the distribution of the orientation angles was broad. This was because the cooling rate at the cooling step was the highest among all the zones in the melted area. All the samples prepared in this study were fabricated by liquid-phase sintering. For specimens prepared by solid-state sintering, which is a conventional method for sintering ceramics, crystal precipitation and growth occurs mainly during the sintering step and the cooling step after it. However, the samples prepared in this study were melted and cooled quickly and within a short period. Therefore, the grain sizes and orientations of the samples in this study varied widely from those of the specimens prepared by solid-phase sintering. Moreover, because zone (D) was located on the surface, heterogeneous nucleation growth occurred there, as was the case for zones (A) and (C), and this influenced the grain sizes and orientations of the samples as well. In addition, cracks were noticed in the grain boundary in this zone. These had an effect on the differences in the CTE caused by the rate of random variations in the grain size and orientation of adjacent grains. Subsequently, it is highly likely that the cracks occurred because of the thermal stress caused by this difference in the CTE [21,22].

As for zone (E), epitaxial growth occurred on the crystal plane in the area that did not undergo melting. In this case, the angles of the crystal faces in the unmelted area influenced the orientation angles of the crystal faces of this zone. In addition, as this zone was inside the melted area, the cooling rate was low. Thus, grain growth occurred with ease. Moreover, similar to the case of zone (C), the amount of Nb deposited in zone (E), which acts as grain growth inhibitor, was low. Therefore, the average grain size and aspect ratio were large.

Furthermore, openings, which were different from cracks, were seen to exist in the grain boundaries at the center of the melted area (the area where zones (B), (C), and (E) intersected). It is considered that the openings occurred owing to the thermal stresses, which were caused by the anisotropy of the CTE of Al_2O_3. As the grains in zones (B), (C), and (E) intersect in this area, the difference in their orientations were large, as shown in Fig. 5. If grains of different orientations exist adjacent to each other, thermal stress also occurs because there are differences in the CTEs [21,22]. When considering all the three dimensions, since the difference in CTE is large, the thermal stress also becomes large. Therefore, it is likely that the openings in the grain boundaries developed during the cooling step after the melting step. It is also highly likely that these were attributable to the gases, i.e., the occluded and melting gases from $A1_2O_3$ and the occluded gases from the Nb wire emitted during the melting process that remained half-way through the grain-boundary diffusion process. However, at present, it is not certain whether the thermal stress or the gases led to the development of the openings.

3.2. Effects of annealing on the crystal structure of Al_2O_3

The BSE image of the cross-section of Sample AN is shown in Fig. 9. The grains in this area were very coarse,

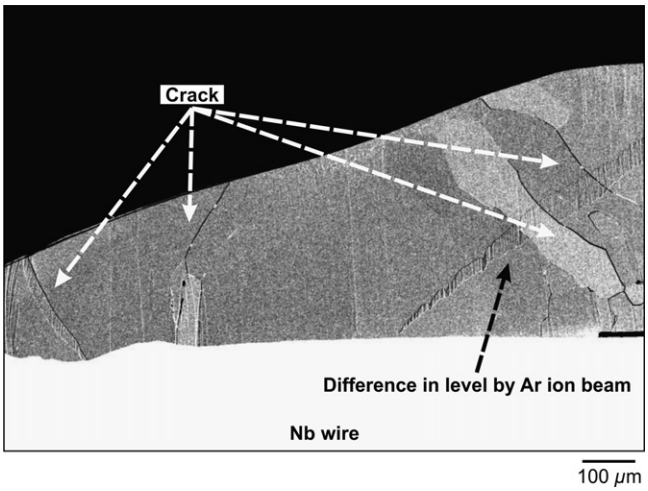

Fig. 9. BSE image of a cross-section of Sample AN.

Table 5
Crystal structure of Sample AN.

Average grain size (μm)	Random variation rate of grain size	Aspect ratio
65.7	1.6	4.5

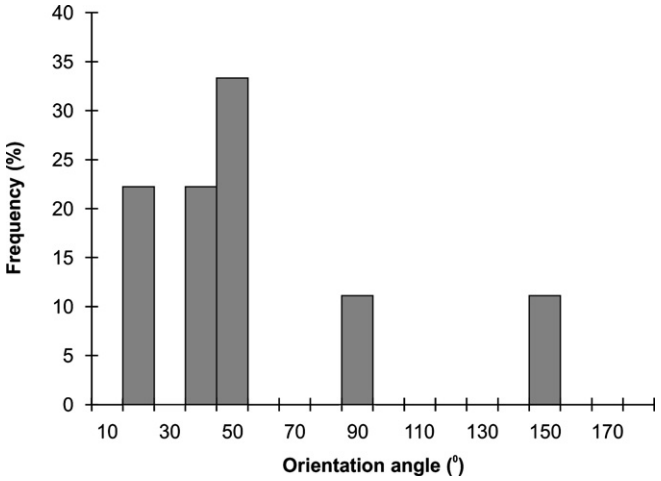

Fig. 10. Distribution of grain orientation angles in Sample AN.

overall, and grain boundary cracks were seen to exist. The values of the average grain size, the rate of random variations in the grain size, and the aspect ratio are given in Table 5. The distribution of the orientation angles is shown in Fig. 10. In addition, the distribution of the size of each grain is shown in Fig. 11. It could be seen that the difference in the distributions of the orientation angles of the grains was large, and the particle size distribution was wide. The formation of a microstructure, that is, the coarsening of the grains, which is an effect of annealing, can be cited as a reason for these phenomena. As to the reason why cracks develop in the grain boundary, it is thought that they are also caused by the coarsening of the grains. The diameter at which "spontaneous cracks" develop in nonisotropic polycrystals is called the "critical particle size." The reason for the development of cracks at the critical particle size is thought to be the thermal stress that is caused by the differences in the CTEs of adjacent grains. The development is also influenced by the grain size distribution and orientation. In the case of Al_2O_3, the value of the critical particle size is 150 μm [22]. As for Sample AN, 10% of the observed grains had sizes that exceeded this value. However, the percentage of grains with sizes closer to the value was also high. Therefore, it is considered that the risk of "spontaneous crack" development in the melted area of Sample AN is high. Moreover, the differences in the orientation angles of the grains were large, and the grain size distribution was wider. For these reasons, the development of grain boundary cracks progressed as the differences in the CTEs further increased the thermal stress.

In the grain boundaries where cracks did not develop, small amounts of a white substance were noticed. The substance was investigated by a mapping analysis performed using an EPMA. The result of the analysis showed that the white substance was Nb, as shown in Fig. 12. However, the amount of Nb noticed in Sample AN was smaller than that seen in Sample RC. It is assumed that Nb reached the outer surface easily because the number of the grain boundary paths

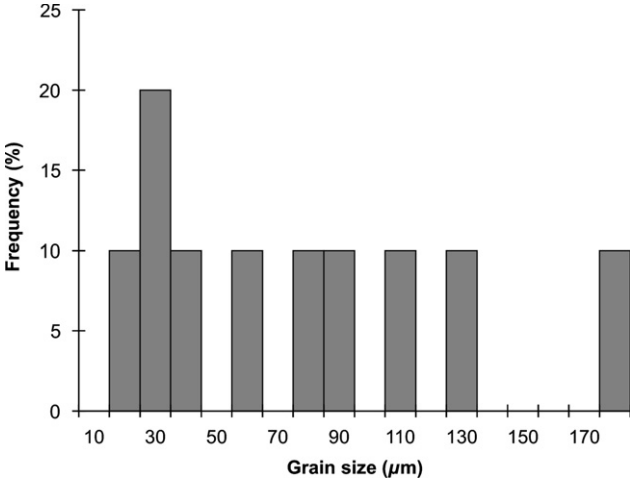

Fig. 11. Distribution of grain sizes in Sample AN.

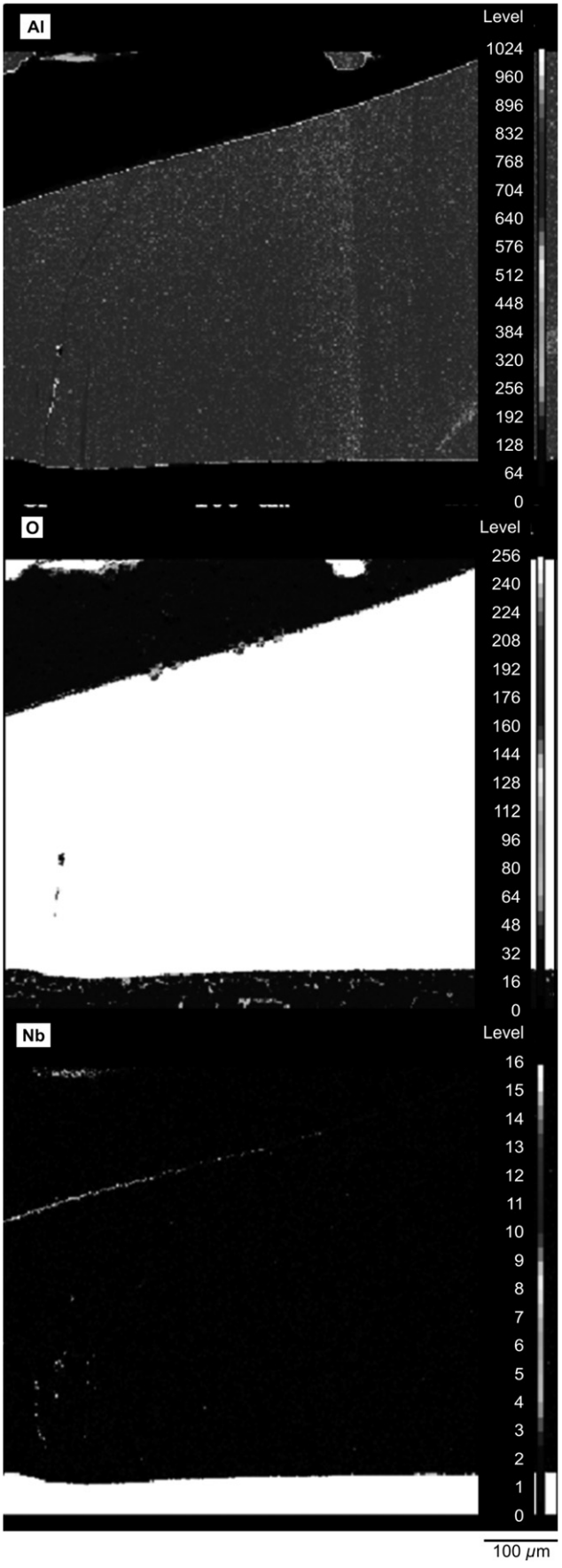

Fig. 12. Result of the EPMA-based analysis of the white substance found between the grain boundaries in Sample AN.

decreased as the grain grew in size. The reason grains became coarse is that the annealing greatly contributed to the process. Furthermore, it is also highly possible that the amount of Nb that was convected and diffused into the melted area did not reach the level that suppresses the grain growth caused by annealing.

Moreover, neither voids nor pores were found to exist. The reason is that the occluded and melting gases from $A1_2O_3$ and the occluded gases from the Nb wire emitted during the melting process, which led to the formation of pores, were diffused through the grain boundary paths and were released outside, when the grain growth progressed because of the annealing.

3.3. Effects of grain boundary deposition of Ta on the crystal structure of Al_2O_3

The observed BSE images of the cross-section of Sample TM are shown in Fig. 13. Using the images, we could confirm that within the melted area, the different zones had different microstructures, and they could be classified into seven zones labeled as (A)–(G). Zone (A) was the zone near the Nb wire; zone (B) was the zone next to zone (A), which was closer to the center of the melted area; zone (C) was the zone next to zone (D), which was closer to the center of the melted area; zone (D) was the zone near foil I of the Ta mesh foil; zone (E) was the zone near the hole of Ta mesh foil; zone (F) was the zone near foil II of the Ta mesh foil; and zone (G) was the zone near the unmelted area. The Ta mesh foil located at the tip of the melted area is the "foil I of the Ta mesh foil," while the Ta mesh foil located on the melted area's side is the "foil II of the Ta mesh foil," and the zone between foils I and II is the "hole of the Ta mesh foil." For all the zones other than (E) and (G), the grains became coarse, and no grain boundaries that could delineate individual grains were noticed. For zone (B), the grains were closer to the center of the melted area, and it tended to form a grain boundary. However, the grain boundary was not complete and was one where the grain growth had just progressed. Thus, even for zone (B), individual grains could not be identified. Only for zones (E) and (G) did clear grain boundaries exist. The values of the average grain size, the rate of random variations in the grain size, and the aspect ratio are shown in Table 6, while the distributions of the orientation angles are shown in Fig. 14. In the case of zone (E), the average grain size, the rate of random variations in the grain size, and the aspect ratio were large. The distribution of

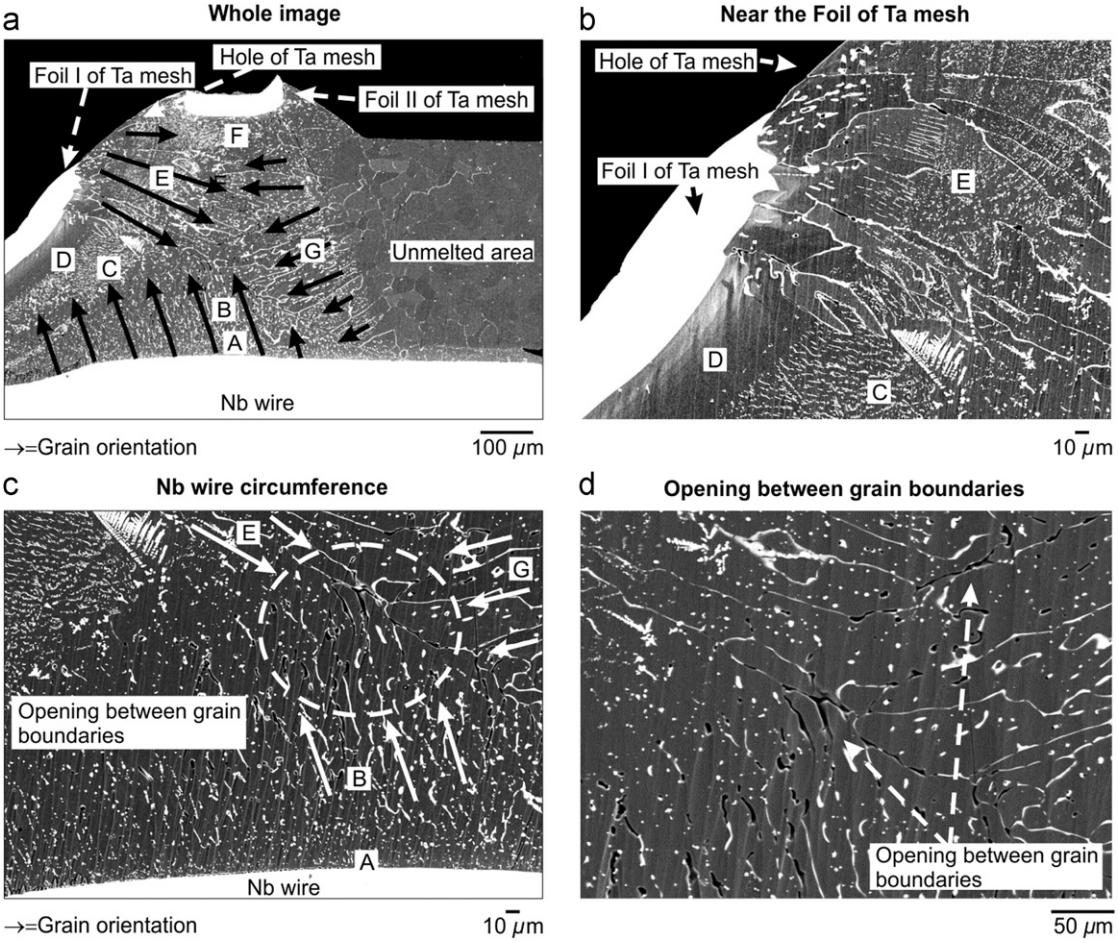

Fig. 13. BSE images of a cross-section of Sample TM. (a) Whole image, (b) Near the foil of Ta mesh, (c) Nb wire circumference and (d) Opening between grain boundaries.

the orientation angles was narrow. For zone (G), the average grain size was smaller than that of zone (E), and the rate of random variations in the grain size and the aspect ratio were larger than those of zone (E). The distribution of orientation angles was narrow as in the case of zone (E).

Some of the reasons for the differences in the microstructures, as shown in Fig. 13, include the effects of thermal conduction during the sealing process by the radiant energy of the YAG laser and the existence of Nb and Ta at the grain boundaries inside the melted area. The thermal conduction consists of two processes in which the Nb wire and Ta mesh foil, respectively, are involved.

3.3.1. The thermal conduction process in which the Nb wire is involved

The process of thermal conduction in which the Nb wire involved is similar to thermal conduction in Sample RC and is explained as follows. The radiant energy from the laser is absorbed by the Nb wire, and the temperature of the Nb wire rises. The absorbed heat is transmitted to the inner surface of the Al_2O_3 capillary by thermal conduction or radiation. At this time, part of the radiant energy from the laser is reflected by the Nb wire and reaches the inner surface of the Ta mesh foil while being transmitted through the Al_2O_3 capillary. At the same time, as the temperature of the Nb wire increases, Nb from the surface of the Nb wire evaporates and is deposited on the inner surface of the Al_2O_3 capillary. This deposition allows the radiant energy from the laser to be absorbed and the temperature of the inner surface of the Al_2O_3 capillary to rise. However, in the case of Sample TM, since Ta mesh foil is wound on the outer surface of the Al_2O_3 capillary, the radiant energy from the laser that reaches the Nb wire is limited to the fraction that can pass through the holes of the Ta mesh foil. Therefore, the temperature of the Nb wire in Sample TM does not rise to the extent it does in Sample RC. To investigate the effect of the radiant energy from the laser that reaches the Nb wire, the sealing of the Al_2O_3 capillary wound with Ta foil was performed using the sealing temperature profile of Sample TM shown in Table 2. The Al_2O_3 capillary did not melt. This indicates that the radiant energy from the laser absorbed by the surface of the Ta mesh foil simply did not allow the temperature to rise to a value high enough to melt the Al_2O_3 capillary. Moreover, it is also assumed that the reflection of the radiant energy from the laser by the Ta mesh foil was also responsible for the low efficiency of the thermal conduction process. This result shows that the absorption in Nb wire of the radiant energy from the laser is essential.

3.3.2. The thermal conduction process in which the Ta mesh foil is involved

The process of thermal conduction in which the Ta mesh foil is involved is explained below. When the laser is energized, absorption of the radiant energy from the laser takes place on the outer surface of the Ta foil mesh and its temperature rises. However, considering that the shape of the outer surface is curved and reflection ratio for the energy from the laser is high, the absorption ratio for the Ta foil mesh is low. Furthermore, as the surface area of the mesh foil is large, heat is also radiated from it. Therefore, the temperature increment ratio of the Ta foil

Table 6
Crystal structure of Sample TM.

Zone	Investigated area	Average grain size (μm)	Rate of random variations in the grain size	Aspect ratio
E	Near the hole of Ta mesh foil	34.0	2.0	4.7
G	Unmelted area	28.3	2.5	7.8

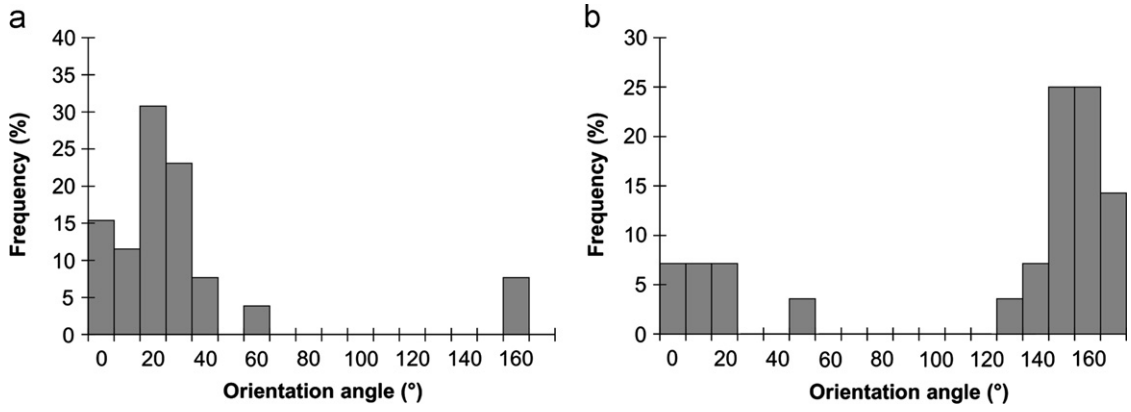

Fig. 14. Distribution of grain orientation angles in Sample TM. (a) E: Near hole of Ta mesh and (b) G: Unmelted area.

mesh becomes lower, and the ratio of the heat transmitted from the Ta mesh foil to the Al_2O_3 capillary by thermal conduction and radiation, respectively, also becomes lower. We postulate that because the thermal conductivity of Al_2O_3 is lower than that of Ta, as shown in Table 4, it takes longer for heat to be transmitted from the Ta mesh foil to the Al_2O_3 capillary. Therefore, while the heat is transmitted to the Al_2O_3 capillary from Ta mesh foil, the radiant heat on the surface of Ta mesh foil occurs. Consequently, the temperature of the capillary is hard to raise. A white substance was noticed in the boundaries of the grains in all the zones in the melted areas. The substance was investigated by mapping analysis performed using an EPMA. The result showed that white substance consisted of Nb in a small concentration and Ta in a large concentration, as shown in Fig. 15. As mentioned in the process of thermal conduction of Sample RC, Nb evaporated from the surface of the Nb wire was deposited on the inner surface of the Al_2O_3 capillary by the radiant energy from the laser, and was convected and diffused into the liquid-phase $A1_2O_3$ when the Al_2O_3 capillary melted. Ta, like Nb, also evaporated from the inner surface of the Ta mesh foil in a similar manner, and was also convected and diffused into the liquid-phase $A1_2O_3$ when the Al_2O_3 capillary melted. As the temperature of the Ta mesh foil at the time of the evaporation is unknown, it is assumed that the temperature reached a value close to the melting point of Ta. In this case, the temperature of the Ta mesh foil at the time of the laser being energized could have reached around 2996 °C, as shown in Table 4. However, as can be seen from the test results using a Ta mesh foil, it is unlikely that the temperature reached this value with the radiant energy from the laser alone. It is quite likely that the temperature of the Ta mesh foil reached around 2996 °C after the Ta mesh foil was heated by the radiant energy reflected by the Nb wire as well. Consequently, we can infer that the temperature of the Ta mesh foil reached a value of around 2996 °C after being heated by both the radiant energy from the laser reaching its surface directly and the radiant energy reflected by the Nb wire. The heat is transmitted from the Ta mesh foil to the Al_2O_3 capillary by thermal conduction or radiation. Ultimately, the Al_2O_3 capillary melts from the synergistic effect of the two thermal conduction processes.

Then, once the laser is switched off, cooling begins, with the outer surface being cooled first, followed by the inner surface. However, the cooling process for Sample TM is different from that for Sample RC and AN because of the influence of the Ta mesh foil. At the start of cooling, the temperature of the Ta mesh foil wound around the outer surface of the melted area is high, so cooling in the area does not occur immediately. In addition, as shown in Table 4, the thermal conductivity of $A1_2O_3$ is lower than that of Ta. Further, the heat capacity of Al_2O_3 is large because the weight of Al_2O_3 in the melted area is high. Therefore, the melted area does not cool readily through the Ta mesh foil. Meanwhile, the temperature of the Nb wire is high immediately after the start of cooling. The Nb wire is also located inside the melted area. Therefore, cooling does not readily occur near the Nb wire as well. On the basis of the process of thermal conduction discussed above, it is inferred that the cooling rate of Sample TM, after melting, is lower than that of Sample AN.

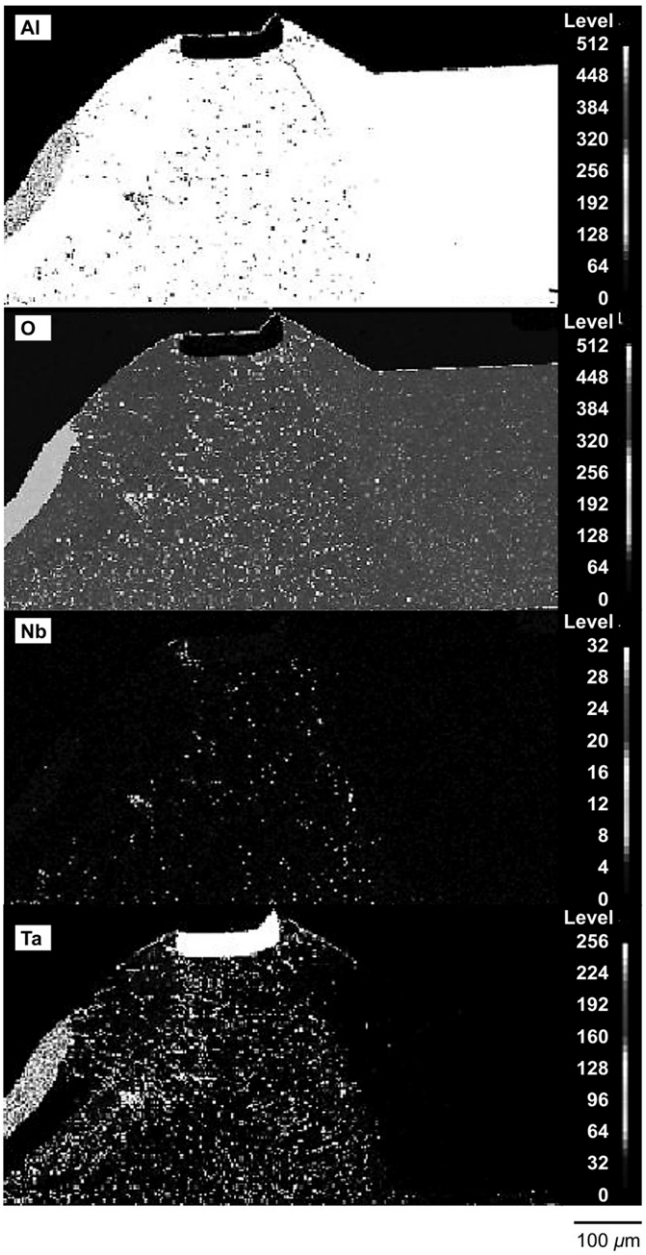

Fig. 15. Result of the EPMA-based analysis of the white substance found between the grain boundaries in Sample TM.

The process of formation for the microstructures in the melted area was discussed taking into account for the above-mentioned process for thermal conduction. Zone (A) exhibited a single coarse grain without grain boundaries. This was due to the high temperature and small cooling rate, given that (A) is located near the Nb wire. In zone (A) of Sample RC, grain boundaries were clearly present. On the basis of this finding, the cooling rate of

zone (A) of Sample TM is at least smaller than that of zone (A) of Sample RC. In addition, as shown in Fig. 15, in addition to zone (A), for all the other zones except for zone (D), Ta or Nb was present inside the grains as well. In particular, the concentration of Ta was high. This is because the total amount of Ta and Nb that convected and diffused into throughout the melted area at the time of the liquid phase was so large that they could not be moved to the grain boundaries when grain growth was taking place at the cooling step. Subsequently, the grain growth proceeded with Ta and Nb still inside the grains.

As for zone (B), although the grain boundaries in it were barely observable, which was in contrast to those in zone (A), they are grain boundaries for grains whose growth was in progress. The corresponding grains were not in a state that allowed them to be observed and classified on the basis of their structure. Assuming that zones (A) and (B) were polycrystalline in structure, the states of the grain boundaries before the commencement of the grain growth is forecasted on the basis of the Ta distribution. The orientation of the grains was from zone (A), i.e., the zone near the Nb wire, to zone (B), which was similar to the orientation of zone (A). Therefore, it is highly possible that except for the difference in grain growth, the microstructures of zones (A) and (B) are similar. This similarity is only because of the difference in the distance from the Nb wire, the heat source, which affects the difference in the cooling rates. As zone (B) is more distant from the Nb wire, its cooling rate is larger than that of zone (A). Therefore, the growth of its grains does not progress with ease. As for the orientation, they were aligned from the Nb wire toward the center of the melted area. Thus, there is a high possibility that thermal distribution may have taken place in the same direction [20], in which case the direction would be the same as that predicted above. Furthermore, it is also highly possible that heterogeneous nucleation of Al_2O_3 grains occurred in zone (A) at the interface with the Nb wire when the grain growth was initiated, and grain growth took place. Therefore, it is considered that the orientation of zone (B) was also influenced by the angles of the crystal faces of the grain nuclei produced by heterogeneous nucleation, in addition to being influenced by the thermal distribution.

As for zone (C), grain boundaries did not exist, and the grains were coarse. The concentrations of Nb and Ta were highest among all the zones in the melted area. This is because Ta and Nb transported to the grain boundaries during grain growth in zone (D) were precipitated on the adjacent zone (C). Moreover, assuming that zone (C) has a polycrystalline structure, the state of the grain boundaries before the grain growth had actually commenced was predicted on the basis of the Ta distribution. The grains were aligned from the Nb wire toward zone (C), and this direction was similar to that of zone (B). Therefore, it is assumed that zone (C) has a microstructure similar to that of zone (B), and the two were different only with regard to the concentrations of Nb and Ta.

Zone (D) contained a single coarse grain without grain boundaries. Furthermore, neither Ta nor Nb was present inside the grain. This indicates that the self-diffusion of Al_2O_3 during the sealing process was larger than that in the other zones in the melted area. In other words, the melting temperature was higher compared to those for the other zones. Given that the cooling rate of this zone is smaller compared to those of the other zones owing to the presence of the Ta mesh foil, grain growth was promoted. Lastly, Nb and Ta were transported to zone (C).

Zone (E) was polycrystalline in nature and had grain boundaries that could be observed clearly. The grains in this zone grew from the hole and the edges of the hole of the Ta mesh foil toward the center of the melted area. At the edge of the hole, the interfacial energy is high; in the hole (i.e., the section where $A1_2O_3$ in the melted area is exposed), the surface energy is high. Therefore, there is a high possibility that heterogeneous nucleation of grains of Al_2O_3 occurred. Moreover, the average grain size and the rate of random variations in the grain size were large. However, because this zone is near the Ta mesh foil, cooling is achieved more readily compared to zones (D) or (F). Therefore, it is inferred that excessive grain growth did not take place. In addition, the grains were oriented toward the center of the melted area from this zone. Therefore, it is highly possible that heat was distributed in this direction [20]. This is almost identical to the thermal distribution discussed above. Given the results for zone (D), the area where the radiant energy of the laser was the highest of all the zones in the melted area, that is, the zone where the temperature rose to the highest value was zone D.

Zone (F) was similar to zone (D) in that there was a single coarse grain without grain boundaries near the Ta mesh foil. However, unlike in zone (D), Nb and Ta were present inside the grain. This is because the melting temperature for this zone is lower compared to that of zone (D) near the Ta mesh foil. Therefore, the self-diffusion of Al_2O_3 during the sealing process becomes lower than that for zone (D), and thus the Nb and Ta were not removed from this zone. However, the cooling rate is lower compared to those of the other zones in the melted area because of the Ta mesh foil. Therefore, it is assumed that the grain growth was promoted.

Zone (G) was polycrystalline, and its grain boundaries could be clearly observed. Moreover, the aspect ratio was large. This was because of the epitaxial growth generated on the crystal surface of the unmelted area. Therefore, the narrowness of the distribution of the orientation angles affects the angles of the crystal faces in the unmelted area. In addition, as this zone is neither located on the Ta mesh foil nor near the Nb wire, the temperature at the time of melting is relatively low. Thus, unlike for zone (A) and (D), excessive grain growth did not take place.

Moreover, as shown in Fig. 13, openings, which were different from cracks, were present in the grain boundaries located at the center of the melted area. It is considered

that the openings occurred owing to thermal stresses, which were caused by the anisotropy in the CTE of Al_2O_3, like in Sample RC. Zones (B), (E), and (G) intersect in this area. The orientations of zones (E) and (G) are shown in Fig. 14. The orientations of these zones were different. In addition, the grain size could not be observed because zone (B) exhibited grain boundaries for grains whose growth was in progress. However, the orientation was measured assuming that zone (B) was polycrystalline in structure. The average value of the orientation angle was 72°, which was different from the values for zones (E) and (G). If grains of different orientations are adjacent to each other, thermal stress occurs because of a difference in the CTEs during cooling after the melting process [21,22]. Moreover, the crystallization of this area is highly likely to result in a plate-like crystal. When taking a three-dimensional approach, since the difference in the CTEs is large, the thermal stress also becomes large. Therefore, it is likely that the openings in the grain boundaries developed during the cooling step after the melting step. There is also a high possibility that these were due to the gases, i.e., the occluded and melting gases from $A1_2O_3$ and the occluded gases from the Nb wire emitted during the melting process that remained half-way through the grain-boundary diffusion process. However, at present, it is not certain whether the thermal stress or the gases led to the development of the openings.

Furthermore, neither voids nor pores were present inside the melted area. This affects the annealing during the cooling step that is a part of the sealing process. Therefore, the gases (i.e., the occluded and melting gases from $A1_2O_3$, the occluded gases from the Nb wire) emitted during the melting process, which could be the cause of the voids and pores, passed through the grain boundary paths and were diffused and eliminated. However, in spite of the annealing performed, the coarsening of the grains did not take place. This is because, unlike in the case of Sample AN, the large amount of Ta present acted as a growth inhibitor as it was convected and diffused into the melted area.

4. Conclusions

This study proposed a new method for forming a seal between a Nb wire and an Al_2O_3 capillary melted by the radiant energy from a YAG laser, without using a glass frit. However, cracks or voids developed inside the melted Al_2O_3 capillary. Therefore, in order to obtain a better seal, the Al_2O_3 microstructure was controlled, and optimization of the sealing conditions was carried out. Through this study, it was found that it is important to control the Al_2O_3 grain size in the melted area along with the random variations in its values, aspect ratio, and orientation in order to suppress the grain boundary cracks. Furthermore, it was found that annealing during the cooling step of the sealing process is necessary in order to eliminate voids. The grain boundary deposition of large amounts of a high-melting-point metal such as Ta was found to be effective in controlling grain growth.

Thus, the optimization of the Al_2O_3 microstructure was achieved by controlling these factors, and this led to the optimization of the seal.

References

[1] S. Jungst, D. Lang, M. Galvez, Improved arc tubes for ceramic metal halide lamps, in: Proceedings of the 9th International Symposium on the Science and Technology of Light sources, New York, USA, August 12–16, 2001.
[2] T.G.M.M. Kappen, Ceramic metal halide lamps: a world of lighting, in: Proceedings of the 9th International Symposium on the Science and Technology of Light sources, New York, USA, August 12–16, 2001.
[3] S.M. DeCarr, J.C. Grande, M. Gyor, I. Laher, D.J. Lovett, J. Meszaros, Characterizing metal-to-ceramic seals for high intensity discharge lamps, in: Proceedings of the 9th International Symposium on the Science and Technology of Light sources, New York, USA, August 12–16, 2001.
[4] L. Yuzhu, G. Zhiting, Z. Weidong, H. Huaqiang, Study on thermal expansion coefficient of sealing materials for ceramic metal halide lamps, Journal of Rare Earths 25 (2001) 249–252.
[5] G. Dobos, K.V. Josepovits, Z. Toth, I. Csanyi, L. Kocsanyi, Surface analytical study of the ceramic-metal bond in the electrical feed-through of high pressure sodium lamps, in: Proceedings of the 9th International Symposium on the Science and Technology of Light sources, New York, USA, August 12–16, 2001.
[6] H. Takashio, Translucent aluminum oxide-to-niobium metal seals by solder glass in the system $CaO–Al_2O_3–SiO_2–MgO$, Yogyo-Kyokai-Shi 80 (1972) 163–172.
[7] H. Takashio, Translucent aluminum oxide-to-niobium metal seals using a crystalline solder in the system $CaO–Al_2O_3–MgO–B_2O_3$, Yogyo-Kyokai-Shi 84 (1976) 420–425.
[8] H. Takashio, Translucent aluminum oxide-to-niobium metal seals by a modified solder glass technique using an adhesive in the system $CaO–Al_2O_3–SiO_2–MgO$, Yogyo-Kyokai-Shi 82 (1974) 248–256.
[9] N. Brates, D. Goodman, J. Maya, Y. Nishimura, N. Takeuchi, Salt-frit reactions in ceramic metal halide lamps, in: Proceedings of the 9th International Symposium on the Science and Technology of Light sources, New York, USA, August 12–16, 2001.
[10] Z. Toth, A. Juhasz, B. Nyiri, Evaluation of the mechanical properties of hid sealing during ageing, in: Proceedings of the 9th International Symposium on the Science and Technology of Light sources, New York, USA, August 12–16, 2001.
[11] Z. Toth, Z. Koltani, G. Steinbach, A. Juhasz, K. Varadi, Residual stress anisotropy in high pressure sodium lamp seals, in: Proceedings of the 9th International Symposium on the Science and Technology of Light sources, New York, USA, August 12–16, 2001.
[12] S. Morozumi, M. Kikuchi, T. Nishino, Bonding mechanism between alumina and niobium, Journal of Materials Science 16 (1981) 2137–2144.
[13] A. Khangar, E. Kenik, N. Dahotre, Microstructure and microtexture in laser-dressed alumina grinding wheel material, Ceramics International. 10.1016/j.ceramint.2004.08.013.
[14] G.C. Wei, Transparent ceramic lamp envelope materials, Journal of Physics D: Applied Physics 38 (2005) 3057–3065.
[15] Y. Terada, Thermophysical properties of Rh_3X for ultra-high temperature applications, Platinum Metals Review 50 (2006) 69–76.
[16] TAPP version 2.2 (E S MICROWARE, Inc.).
[17] A. Ingenito, C. Bruno, Using aluminum for space propulsion, Journal of Propulsion and Power 20 (2004) 1056–1063.
[18] K. Das, S. Das, Diffusional, Reactions during processing of TIMETAL $21S/Al_2O_3$ composites, Metallurgical and Materials Transactions A 30A (1999) 1437–1447.

[19] M. Nawa, T. Sekino, K. Niihara, Fabrication and mechanical behaviour of Al_2O_3/Mo nanocomposites, Journal of Materials Science 29 (1994) 3185–3192.
[20] B.S. Yilbas, C. Karatas, A.F.M. Arif, B.J.Abdul Aleem, Laser control melting of alumina surfaces and thermal stress analysis, Optics & Laser Technology 43 (2011) 858–865.
[21] V.D. Krstic, Critical grain size/preexisting flaw size relations in anisotropic brittle solids, Journal of the American Ceramic Society 66 (1983) 726–729.
[22] V.D. Krstic, Fracture of brittle solids in the presence of thermoelastic stresses, Journal of the American Ceramic Society 67 (1984) 589–593.